A COMPARISON OF IMAGING CONDITIONS FOR WAVE-EQUATION SHOT-PROFILE MIGRATION

J. Schleicher, J. C. Costa, and A. Novais

email: *js@ime.unicamp.br*
keywords: *Imaging condition, wave-equation migration, amplitude*

ABSTRACT

The application of an imaging condition in wave equation shot profile migration is important to provide illumination compensation and amplitude recovery. Particularly for true-amplitude wave-equation migration algorithms, a stable imaging condition is essential to successfully recover the medium reflectivity. We study a set of image conditions with illumination compensation. The imaging conditions are evaluated by the quality of the output amplitudes and the artifacts produced. In numerical experiments using a vertically inhomogeneous velocity model, the most stable of the tested imaging condition divides the up- and downgoing wavefields after inverse Fourier transform.

INTRODUCTION

Shot-profile migration is a method used to construct an image of the earth interior from seismic data. This technique is implemented in two steps. The first step, consist of downward continuing the source and receiver wavefields for each shot position and the second step consist of applying the imaging condition. The imaging step is based on Claerbout's imaging principle (Claerbout, 1971).

The basic imaging condition from Claerbout's imaging principle uses one-dimensional deconvolution between the down- and up-going wavefields, i.e., division in the frequency domain. Since this division is unstable off the reflector position, historically, and for practical reasons, the imaging condition is usually estimated by cross-correlating the down- and up-going wavefields (Claerbout, 1971).

With shot-profile migration (SPM), better images can be obtained by implementing better imaging conditions. The imaging condition can impact both amplitudes and migration artifacts (Valenciano and Biondi, 2003). Particularly for true-amplitude wave-equation migration algorithms, a stable imaging condition correctly applying Claerbout's imaging principle is essential to successfully recover the medium reflectivity.

Valenciano and Biondi (2003) propose a different imaging condition that is based on Claerbout's imaging principle. It consist in deconvolving the receiver wavefield by the source wavefield in two dimensions. This imaging condition satisfies Claerbout's imaging principle. It also improves the resolution of the image and reduces illumination effects in the final the image.

Guitton et al. (2006) present an alternative deconvolutional approach, based on smoothing the autocorrelation of downgoing wavefield in the denominator. The idea is to fill-up the spectral holes of the denominator by neighboring values, instead of some arbitrary number. They show that this new formulation yields better amplitudes and is quite robust and rather insensitive to the choice of parameters for the smoothing windows.

In this paper, we compare a set of different imaging conditions and study their impact on the enhancement of boundary effects and, particularly, on the quality of output amplitudes at different reflector depths.

METHOD

Wave equation migration tries to undo the propagation effects described by the (acoustic) wave equation on the surface data $Q(x_r, y_r; \omega)$ recorded at the receiver at $\mathbf{x}_r = (x_r, y_r, z = 0)$. After Fourier transform, the wave equation reads

$$\left(\frac{\omega^2}{v^2} + \frac{\partial^2}{\partial z^2} + \Delta\right) p(x, y, z; \omega) = -\delta(\mathbf{x} - \mathbf{x}_s), \tag{1}$$

where $\Delta = \frac{\partial^2}{\partial x^2} + \frac{\partial^2}{\partial y^2}$, and where $\mathbf{x}_s$ denotes the source location. The solution of this equation at $\mathbf{x}_r$ must equal the recorded surface data $Q(x_r, y_r; \omega)$, i.e.,

$$p(x_r, y_r, z = 0; \omega) = Q(x_r, y_r; \omega). \tag{2}$$

To map this solution into depth, the Helmholtz equation (1) is generally decomposed into two one-way wave equations. These are

$$\left(\frac{\partial}{\partial z} + i\frac{\omega}{v}\sqrt{1 + \frac{\omega^2}{v^2}\Delta}\right) P_D = 0, \tag{3}$$

with initial condition

$$P_D(x, y, z = 0; \omega) = \delta(\mathbf{x} - \mathbf{x}_s) \tag{4}$$

for the downgoing waves, and

$$\left(\frac{\partial}{\partial z} - i\frac{\omega}{v}\sqrt{1 + \frac{\omega^2}{v^2}\Delta}\right) P_U = 0 \tag{5}$$

with initial condition

$$P_U(x, y, z = 0; \omega) = Q(x, y; \omega) \tag{6}$$

for the upgoing waves.

After propagating the waves from the indicated initial conditions at $z = 0$ into the underground (downgoing waves forward from $t = 0$, upgoing waves backward from $t = t_{\text{max}}$), an imaging condition must be applied in order to obtain the final image. The theoretically correct imaging condition is the division of both wavefields at the reflectors depth in order to recover the reflection coefficient as the amplitude ratio, i.e.,

$$R(x, y, z) = \sum_{j=1}^{N_\omega} \frac{P_U(x, y, z; \omega_j)}{P_D(x, y, z; \omega_j)}\ , \tag{7}$$

where N_ω is the number of frequencies used in the process. Since the reflector position is unknown, this division has to be carried out at all depths, which is rather unstable. Therefore, many different practical imaging conditions have been suggested. Below we give an overview over a number of them and compare their performance on a simple vertical-gradient model with four horizontal interfaces.

IMAGING CONDITIONS

The simplest imaging condition is the one originally proposed by Claerbout (1971). It uses a simple convolution of the up- and downgoing fields, viz.

$$R(x, y, z) = \sum_{j=1}^{N_\omega} P_D^*(x, y, z; \omega_j) P_U(x, y, z; \omega_j), \tag{8}$$

where the asterisk denotes the complex conjugate.

This condition is obtained as a simplification of

$$R(x, y, z) = \sum_{j=1}^{N_\omega} \frac{P_U(x, y, z; \omega_j) P_D^*(x, y, z; \omega_j)}{P_D(x, y, z; \omega_j) P_D^*(x, y, z; \omega_j)}\ , \tag{9}$$

which is obtained from equation (7) by multiplication of numerator and denominator with $P_D^*(x, y, z; \omega_j)$, in order to make the denominator real. Of course, equation (9) does not remedy the division by zero. However, the denominator is now merely a scale factor that does no longer contain any phase information. Thus, if no amplitude information is to be preserved, the denominator can be omitted, leading to imaging condition (8).

Actual implementations of imaging condition (9) retaining the denominator need to apply some stabilization. Here, we have tested two forms. The first one is an additive form, given by

$$R(x, y, z) = \sum_{j=1}^{N_\omega} \frac{P_U(x, y, z; \omega_j) P_D^*(x, y, z; \omega_j)}{P_D(x, y, z; \omega_j) P_D^*(x, y, z; \omega_j) + \varepsilon} , \tag{10}$$

where ε is an additive constant. There are many ways to define its value. A constant value for all depth levels is generally an inadequate choice, leading to insufficient stability or too strong smoothing at different depth levels. In our numerical tests, we used

$$\varepsilon = \varepsilon(\omega, z) = \lambda[\max_{x,y}(|P_D(x, y, z; \omega)|^2)] . \tag{11}$$

In other words, the stabilization is achieved by adding a fraction ($0 < \lambda < 1$) of the maximum of the squared absolute value of the downgoing wavefield at the current depth level to the denominator.

The second one is a low-cut form, given by

$$R(x, y, z) = \sum_{j=1}^{N_\omega} F(x, y, z; \omega_j), \tag{12}$$

where

$$F(x, y, z; \omega) = \begin{cases} \dfrac{P_U(x, y, z; \omega_j) P_D^*(x, y, z; \omega_j)}{\varepsilon}, & \text{if } |P_D(x, y, z; \omega)|^2 \leq \varepsilon \\ \dfrac{P_U(x, y, z; \omega_j) P_D^*(x, y, z; \omega)}{P_D(x, y, z; \omega) P_D^*(x, y, z; \omega)}, & \text{if } |P_D(x, y, z; \omega)|^2 > \varepsilon \end{cases} , \tag{13}$$

where ε is again defined by equation (11). In other words, stabilization is achieved by substitution of all values of the denominator smaller than a fraction of the maximum value of the wavefield at the current depth level by that value.

A corresponding stabilization can also be realized using the original complex division (7). We have tested four forms of such a stabilization. The first and second ones are again additive forms, viz.

$$R(x, y, z) = \sum_{j=1}^{N_\omega} \frac{P_U(x, y, z; \omega_j)}{P_D^*(x, y, z; \omega_j) + \varepsilon} , \tag{14}$$

where the additive values are taken as fractions of the maximum or mean absolute values of the wavefield at the current depth, i.e.,

$$\varepsilon = \varepsilon(\omega, z) = \lambda \max_{x,y}(|P_D(x, y, z; \omega)|) \tag{15}$$

and

$$\varepsilon = \varepsilon(z) = \lambda \frac{1}{N_\omega} \sum_{j=1}^{N_\omega} |P_D(x, y, z; \omega_j)| , \tag{16}$$

respectively.

The third and fourth ones are low-cut forms, viz.,

$$R(x, y, z) = \sum_{j=1}^{N_\omega} F(x, y, z; \omega_j), \tag{17}$$

where

$$F(x,y,z;\omega) = \begin{cases} \dfrac{P_U(x,y,z;\omega_j)}{\varepsilon}, & \text{if } |(P_D(x,y,z;\omega)| \le \varepsilon \\ \dfrac{P_U(x,y,z;\omega_j)}{P_D^*(x,y,z;\omega)}, & \text{if } |P_D(x,y,z;\omega)| > \varepsilon \end{cases} , \tag{18}$$

using the same values for ε as defined in equations (15) and (16).

Recently, imaging conditions using lateral smoothing have been proposed. We have tested four such conditions. The first one uses a smoothed denominator in equation (7), i.e.,

$$R(x,y,z) = \sum_{j=1}^{N_\omega} \frac{P_U(x,y,z;\omega_j)}{\ll P_D(x,y,z;\omega_j) \gg} , \tag{19}$$

where the smoothing operator is

$$\ll P_D(x_r,y_s,z;\omega) \gg = \sum_{k=r-n_x}^{r+n_x} \sum_{l=s-n_y}^{s+n_y} P_D(x_k,y_l,z;\omega) . \tag{20}$$

Here n_x and n_y represent the size of the smoothing windows in the x and y directions.

Correspondingly, also the denominator in equation (9) can be smoothed. This yields our next imaging condition, viz.

$$R(x,y,z) = \sum_{j=1}^{N_\omega} \frac{P_U(x,y,z;\omega_j)P_D^*(x,y,z;\omega_j)}{\ll P_D(x,y,z;\omega_j)P_D^*(x,y,z;\omega_j) \gg} . \tag{21}$$

The next two imaging conditions use corresponding smoothing also in the numerator. In formulas,

$$R(x,y,z) = \sum_{j=1}^{N_\omega} \frac{\ll P_U(x,y,z;\omega_j) \gg}{\ll P_D(x,y,z;\omega_j) \gg} \tag{22}$$

and

$$R(x,y,z) = \sum_{j=1}^{N_\omega} \frac{\ll P_U(x,y,z;\omega_j)P_D^*(x,y,z;\omega_j) \gg}{\ll P_D(x,y,z;\omega_j)P_D^*(x,y,z;\omega_j) \gg} . \tag{23}$$

As another image condition, we propose to divide the complete convolutions of the up- and downgoing wavefields at the current depth level after inverse Fourier transform at $t = 0$. In symbols, the proposed image condition reads

$$R(x,y,z) = \frac{U(x,y,z)}{D(x,y,z)} , \tag{24}$$

where

$$U(x,y,z) = \sum_{j=1}^{N_\omega} P_U(x,y,z;\omega_j)P_D^*(x,y,z;\omega_j) \tag{25}$$

and

$$D(x,y,z) = \sum_{j=1}^{N_\omega} P_D(x,y,z;\omega_j)P_D^*(x,y,z;\omega_j) . \tag{26}$$

This imaging condition is actually borrowed from time-domain reverse time migration using the full wave equation.

It turns out that equation (24) is a rather stable imaging condition that generally does not need further stabilization. Only at the corners of the migrated image, very far from sources and receivers, some problems may occur. Because of the location of these problems, it is sufficient to avoid these areas. Alternatively, we have tested the slightly modified form

$$P(x,y,z;\omega) = \begin{cases} \dfrac{U(x,y,z)}{D(x,y,z)}, & \text{if } |D(x,y,z)| > \varepsilon \\ 0 & \text{else} , \end{cases} \tag{27}$$

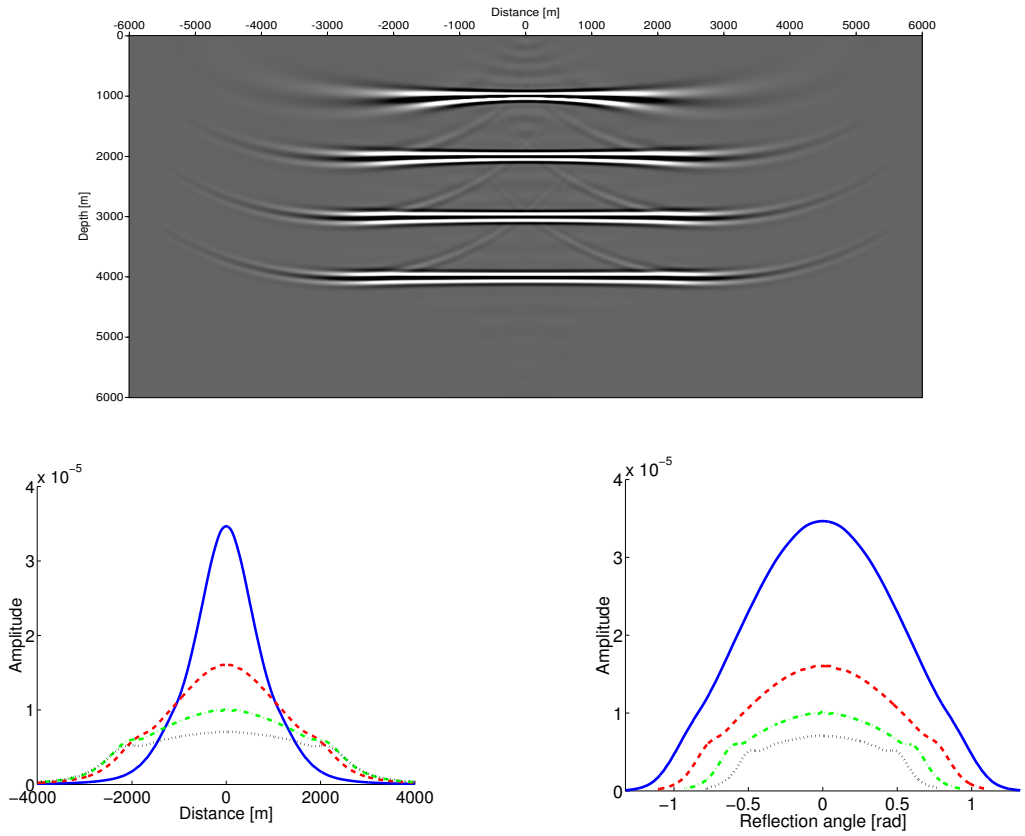

Figure 1: Top: Image using condition (8). Bottom: Amplitude along reflector images as function of offset (left) and angle (right).

where

$$\varepsilon = \varepsilon(z) = \max\{10^{-6}, 0.05 \max_{x,y}(|(D(x,y,z;\omega)|)\} \; . \tag{28}$$

Note that conditions (24) and (27) can be easily generalized to incorporate the time-shift imaging condition of Sava and Fomel (2006). All that needs to be done is calculation of the inverse Fourier transforms in the numerator and denominator with opposite time shifts.

NUMERICAL EXPERIMENTS

We have tested the above 13 different imaging conditions on a synthetic data set for a model with four horizontal reflectors in a vertically inhomogeneous background model with a vertical gradient of 0.2/s. The employed migration was a common-shot phase-shift migration Gazdag (1978, 1980). Note that the same migration was applied in all cases, only varying the imaging condition. For simplicity, the numerical experiments were carried out in two dimensions.

The following figures depict the resulting depth-migrated image using the true velocity distribution, and the amplitude along the four reflector images as a function of offset and angle. Amplitudes along the first, second, third, and forth reflector are depicted as solid blue, dashed red, dash-dotted green, and dotted black curves, respectively.

Figure 1 shows the results of imaging condition (8). We immediately note the different amplitude at the different reflectors. This is a consequence of omitting the denominator. As we will see below, all other tested imaging conditions provide much better calibration between reflectors at different depths. An advantage of the simple imaging condition is its suppression of migration artifacts. This becomes immediately clear when comparing Figure 1 to Figure 2 that shows the corresponding results for imaging condition (10). Here, we chose $\lambda = 0.1$ in equation (11). While the different reflector images are much

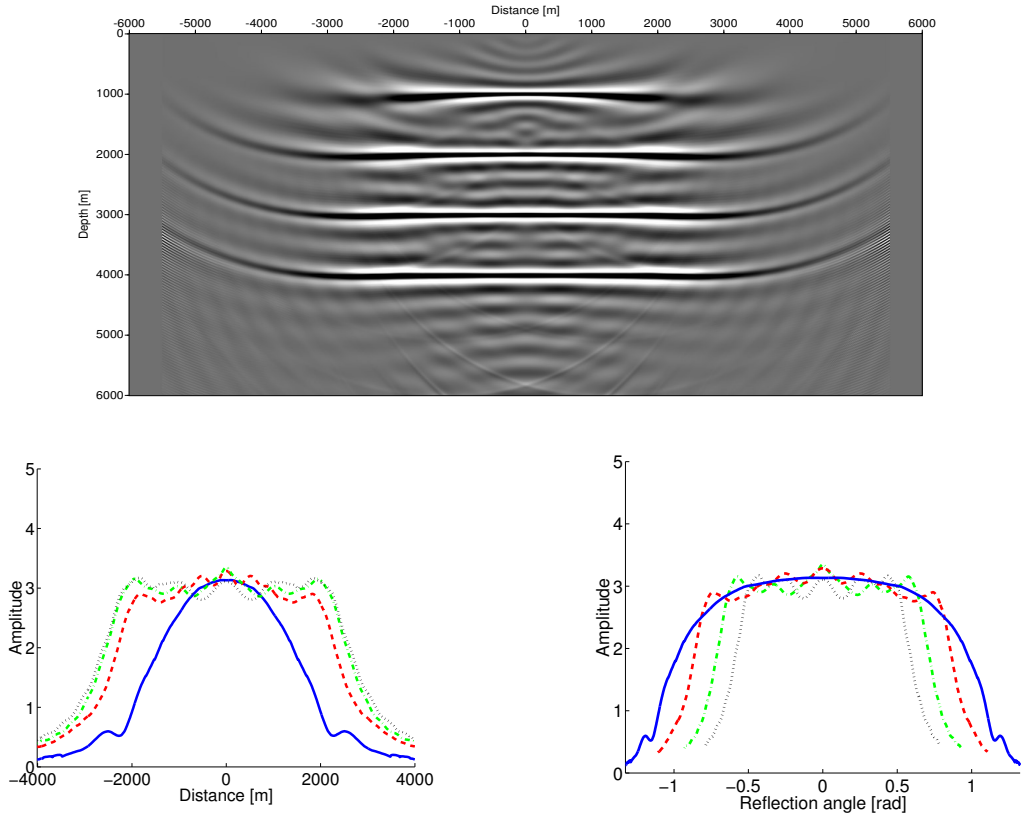

Figure 2: Top: Image using condition (10). Bottom: Amplitude along reflector images as function of offset (left) and angle (right).

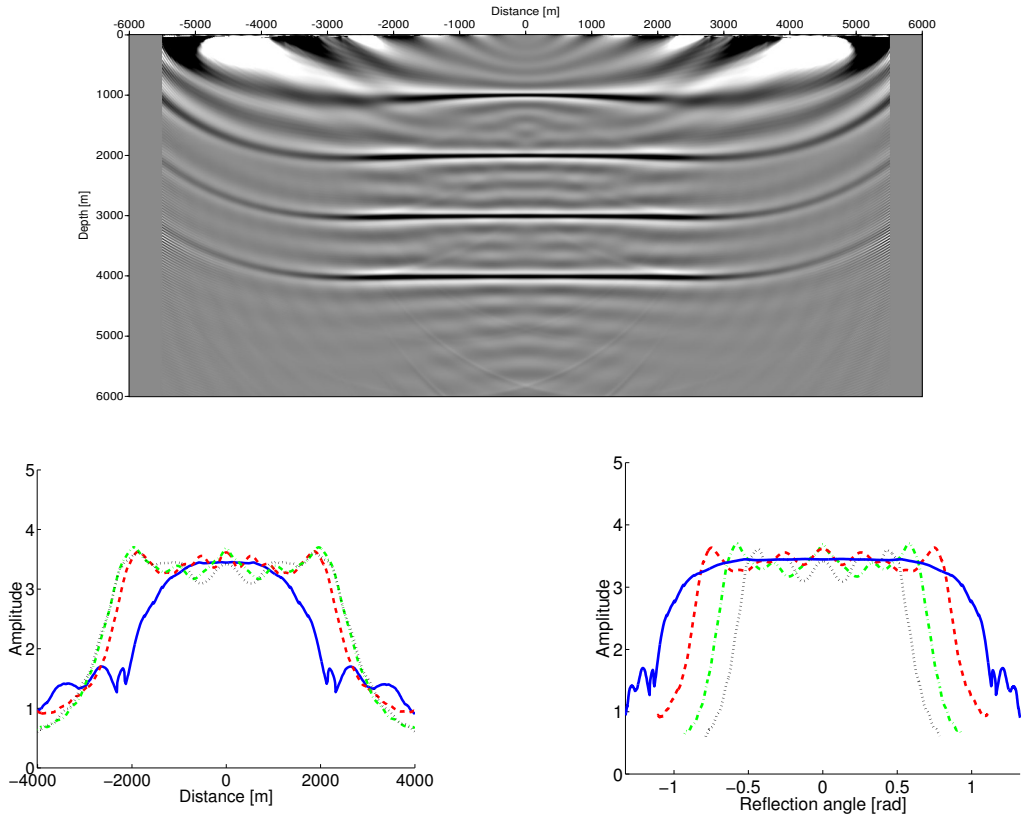

Figure 3: Top: Image using condition (12). Bottom: Amplitude along reflector images as function of offset (left) and angle (right).

better equalized, the migration artifacts are strongly enhanced. This is a general drawback that all imaging conditions relying on a division suffer from, though the degree of enhancement varies. In Figure 2, the strong migration artifacts even lead to a ringing of the amplitudes along the reflector. Note that different scale of migration amplitudes as compared to those in Figure 1. This amplitude scaling is achieved by the division by the downgoing wavefield.

The results of imaging condition (12) are depicted in Figure 3. The deterioration of the quality near the surface is obvious. Deeper down, the behaviour is almost identical to that of condition (10). The main effect seem to be a slightly better recovery of constant amplitudes along to top reflector, as well as a somewhat higher amplitude. This shows that different imaging conditions and their different regularizations may have different effects on the amplitudes. These effects must be taken into account when implementing the amplitude corrections of Zhang et al. (2003, 2005), which have not been considered for the present investigation.

The next imaging conditions to be tested were condition (14) with ε from equations (15) and (16). The results are depicted in Figures 4 and 5, respectively. Again, in both migrated images, the strongest migration artifacts appear close to the surface. Additionally, we note strong circular migration artifacts. Deeper down, the behaviour is similar to that in the previous figures. Figure 4, the maximum migration angle appears as a strong limitation of the migrated image. This causes the amplitudes outside the correctly migrated domain to become random numbers. The corresponding region in Figure 5 resembles more closely that of Figure 3. Still, the amplitudes are more strongly affected from migration artifacts than those in Figure 3.

The results of testing condition (17) with ε from equations (15) and (16) are depicted in Figures 6 and 7, respectively. These imaging conditions treat the migration artifacts slightly different. In Figure 6, they are a little weaker. Above the maximum migration angle, all artifacts are suppressed. The artifacts near the surface in Figure 7 again resemble those in Figure 3. In both cases, the amplitudes ripples are weaker than before.

The results of the imaging conditions (19) to (23) that rely on smoothing are depicted in the next four figures. Figures 8 and 9 show the results of conditions (19) and (21), respectively, which smooth only the denominator. Although the migration artifacts are greatly suppressed in the central part of Figure 8, this image creates the worst impression of all our tests. The reflectors are not even migrated to their correct positions. Correspondingly, the amplitudes along the reflector images also show a completely different behaviour than those for the other imaging conditions, both in shape and scale. Note the different scale of the vertical axis in the amplitude plots of Figure 8. The image in Figure 9 looks again very much the same as the ones in Figures 3, 5, and 7. However, the amplitude along the first reflector suffers some distortion as compared to those figures.

Figures 10 and 11 show the results of conditions (22) and (23), respectively, which smooth both the numerator and the denominator. In the image of Figure 10, the migration artifacts are still strong, though less so than in Figure 8. Also, the reflectors are back to their correct position. The amplitudes show some ringing and slight differences between the different reflectors. Figure 11 creates a much better overall impression. Except for the topmost reflector, amplitudes are rather constant and show no ringing at all. Note that this is more or less the expected behaviour, since horizontal smoothing in a vertically inhomogeneous model should have only positive effects. Further tests in laterally inhomogeneous media are necessary to conclude whether horizontal smoothing may have undesirable effects on amplitudes.

Finally, Figures 12 and 13 show the results of the imaging conditions (24) and (27), respectively. For condition (27), we chose $\lambda = 0.05$ in equation (28). In the image of Figure 12 looks much cleaner than all previous images, even though the artifacts close to the surface persist. However, they appear only in the boundary zone of the image where insufficient data are available anyway. Above the central part of the image of the topmost reflector, no artifacts are visible. The amplitudes are very clean, free from ringing, and almost perfectly constant. For the purpose of stacking all migrated shots, the image of Figure 13 is even better. Inside the actual zone where data are available, the image is identical. The different appearance is due to the fact that both images are scaled to their maximum amplitudes, which in Figure 12 are those of the boundary effect. The amplitude graphs of Figures 12 and 13 show that inside the actual migrated image, the amplitudes are identical. Setting the image to zero where the downgoing wavefield is too small actually provides a nice muting of undesired effects outside the actual image. Note that although image conditions (8) and (27) carry out the illumination compensation by division with the downgoing wavefield,

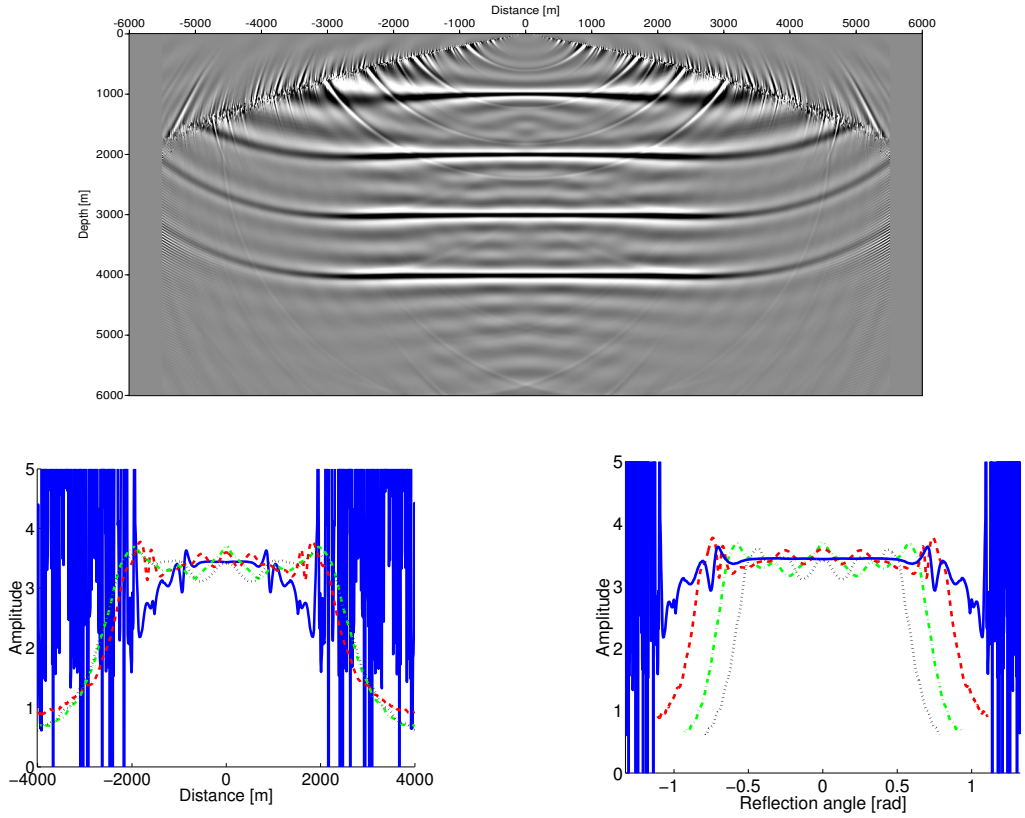

Figure 4: Top: Image using condition (14) with ε from equation (15) using $\lambda = 0.1$. Bottom: Amplitude along reflector images as function of offset (left) and angle (right).

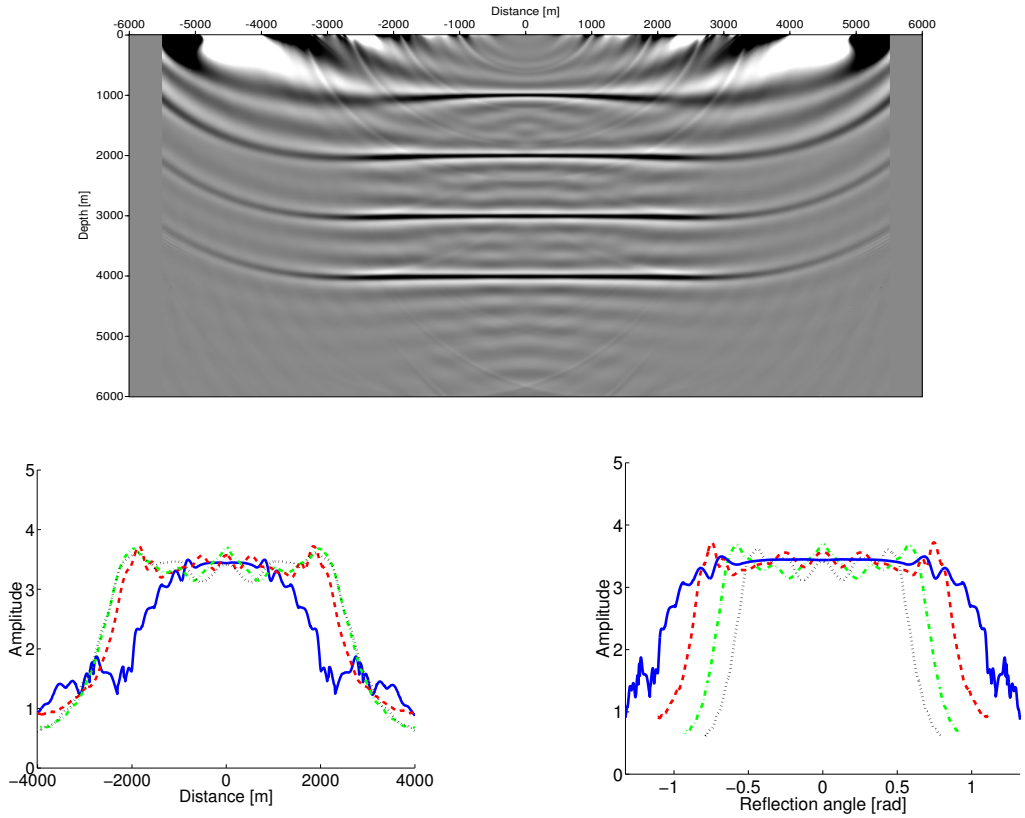

Figure 5: Top: Image using condition (14) with ε from equation (16) using $\lambda = 0.05$. Bottom: Amplitude along reflector images as function of offset (left) and angle (right).

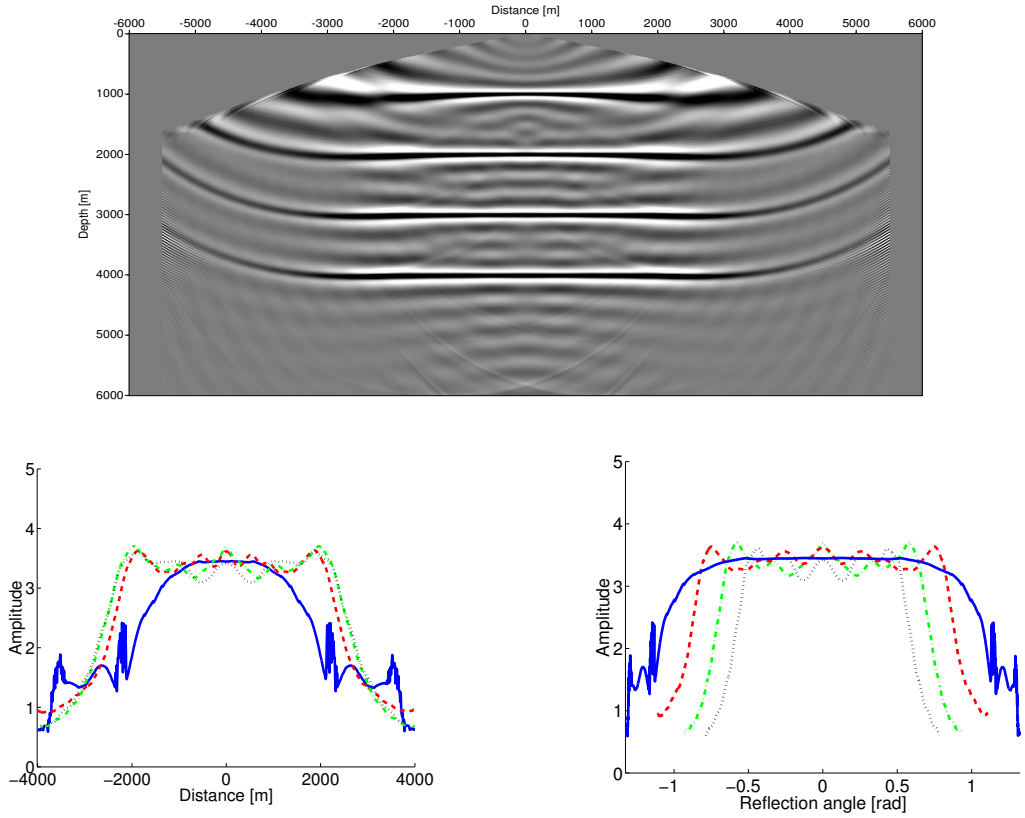

Figure 6: Top: Image using condition (17) with ε from equation (15) using $\lambda = 0.1$. Bottom: Amplitude along reflector images as function of offset (left) and angle (right).

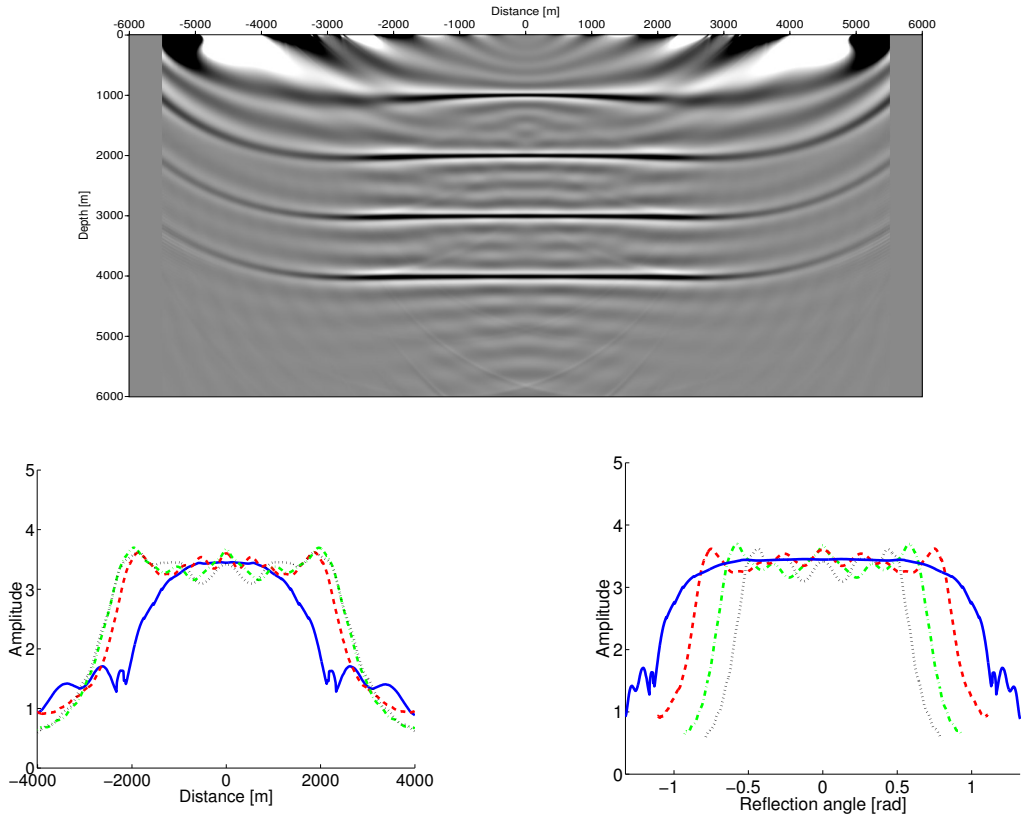

Figure 7: Top: Image using condition (17) with ε from equation (16) using $\lambda = 0.05$. Bottom: Amplitude along reflector images as function of offset (left) and angle (right).

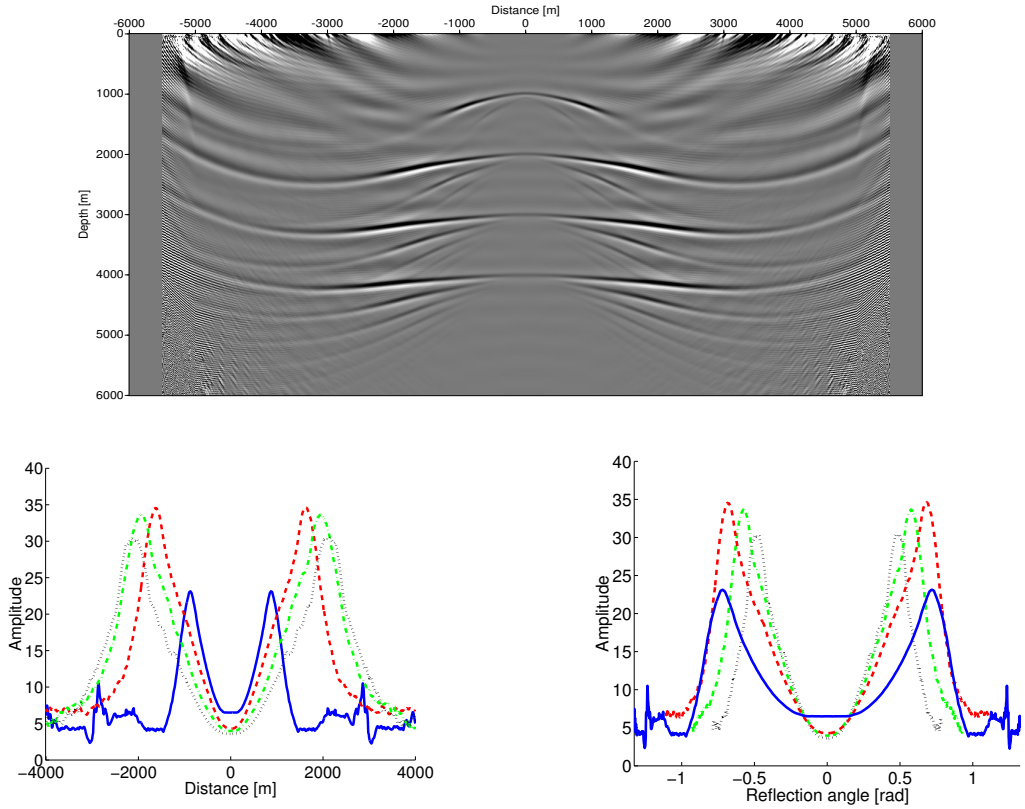

Figure 8: Top: Image using condition (19). Bottom: Amplitude along reflector images as function of offset (left) and angle (right).

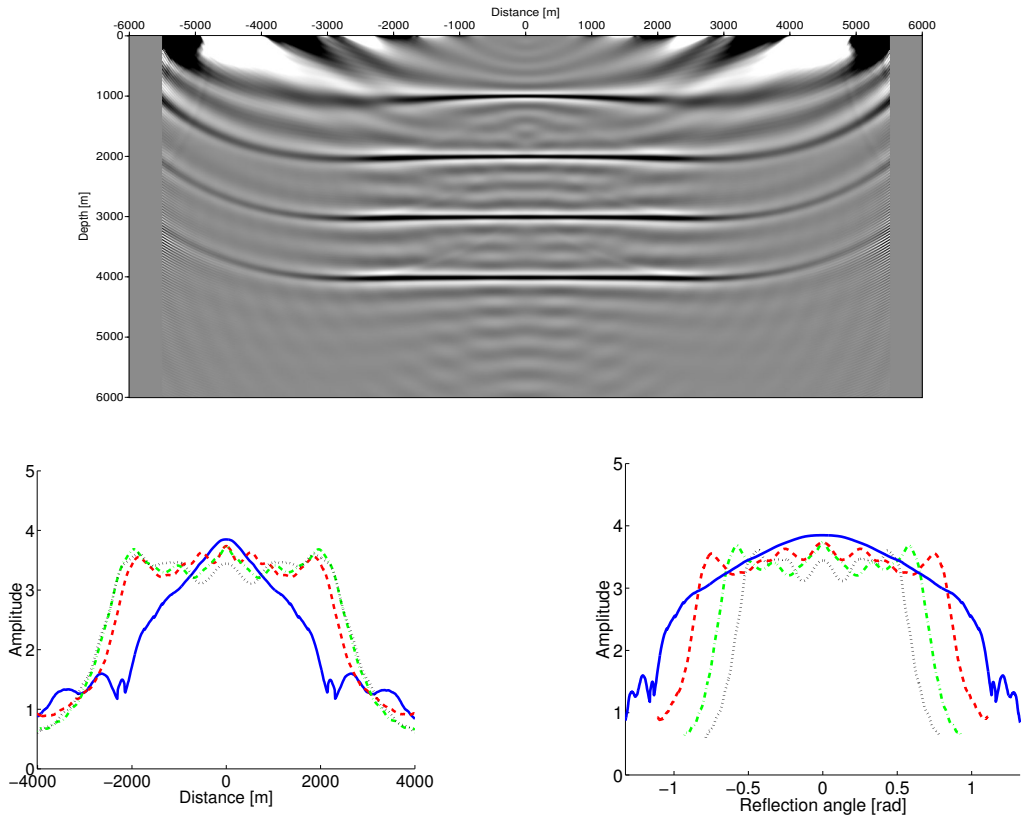

Figure 9: Top: Image using condition (21). Bottom: Amplitude along reflector images as function of offset (left) and angle (right).

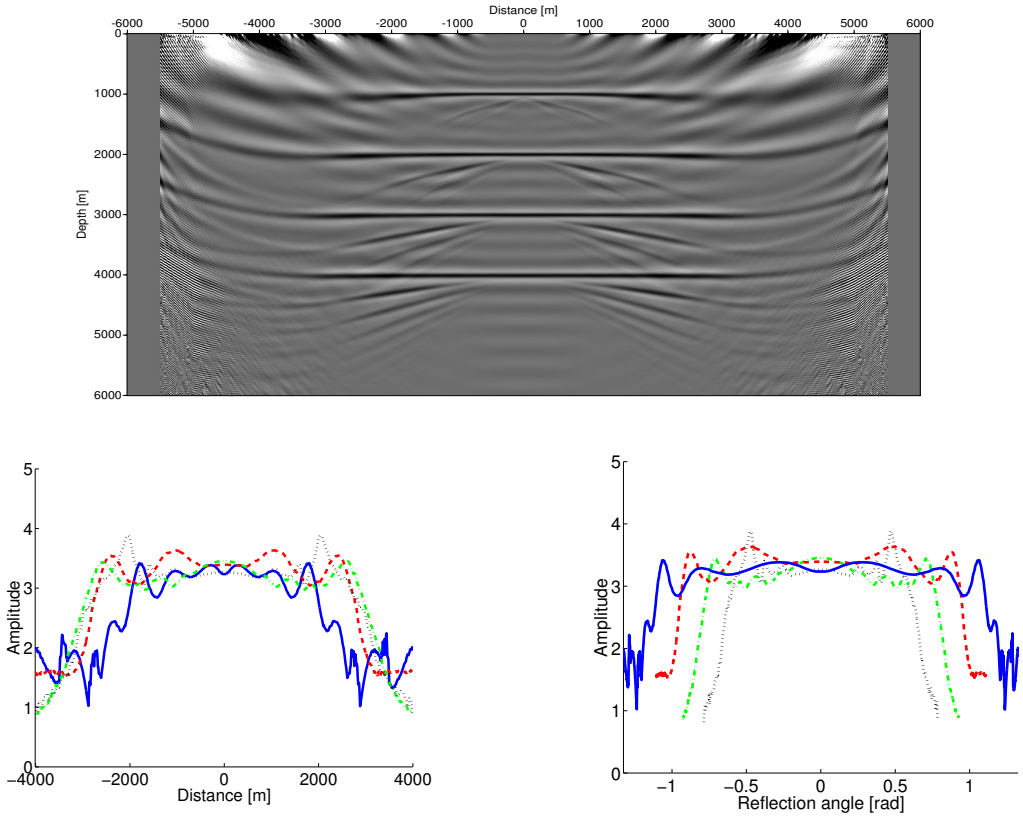

Figure 10: Top: Image using condition (22). Bottom: Amplitude along reflector images as function of offset (left) and angle (right).

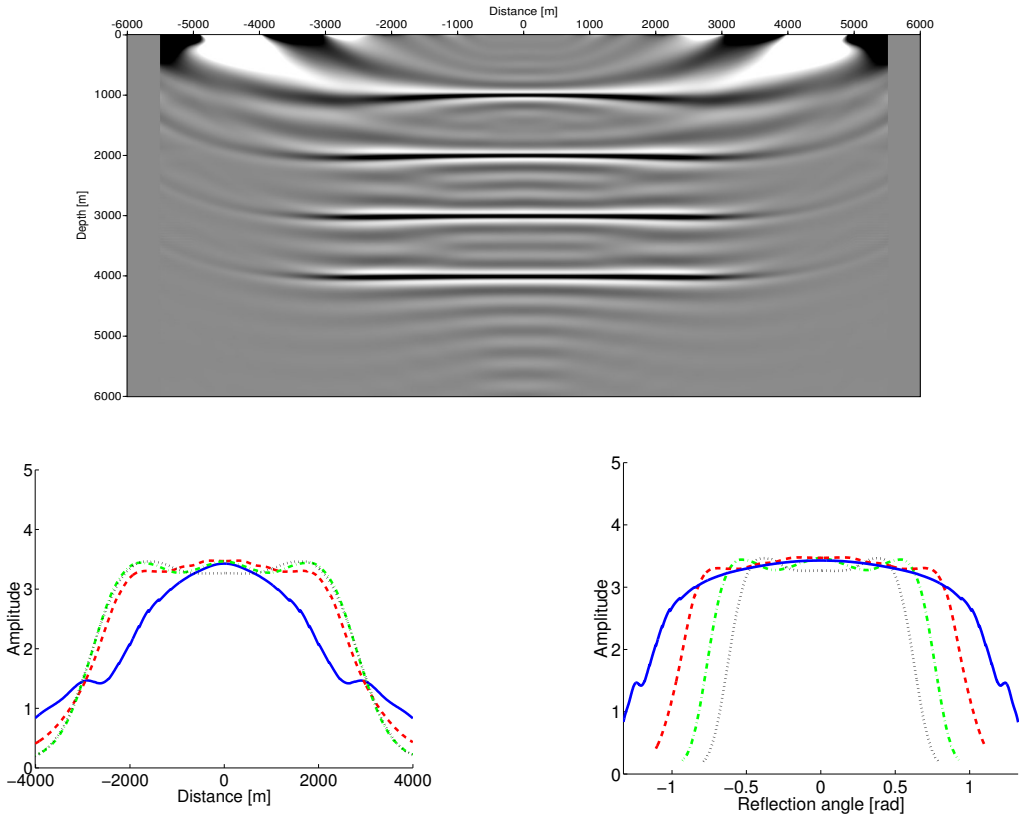

Figure 11: Top: Image using condition (23). Bottom: Amplitude along reflector images as function of offset (left) and angle (right).

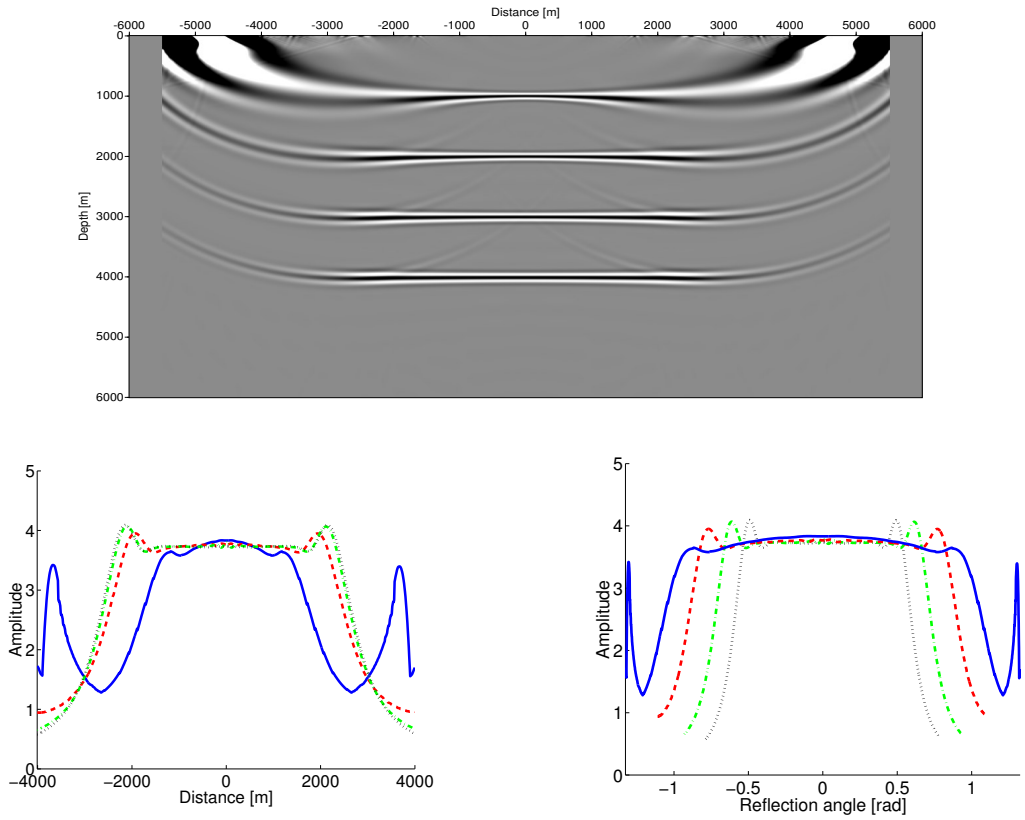

Figure 12: Top: Image using condition (24). Bottom: Amplitude along reflector images as function of offset (left) and angle (right).

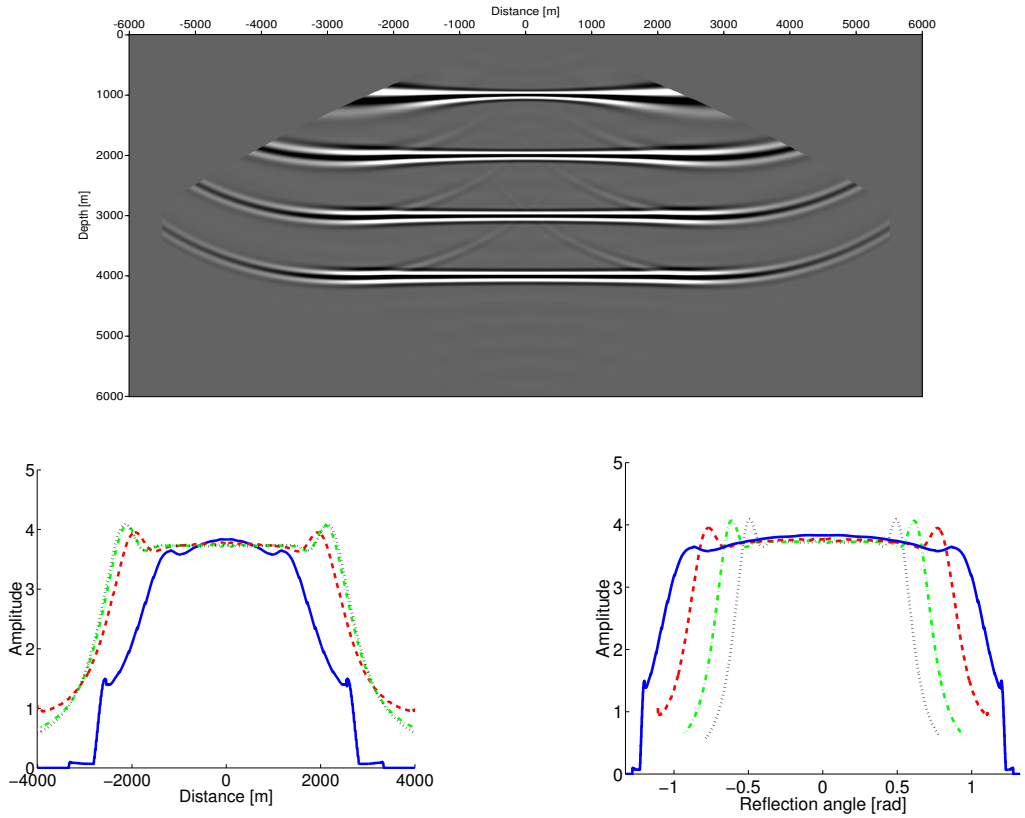

Figure 13: Top: Image using condition (27). Bottom: Amplitude along reflector images as function of offset (left) and angle (right).

the migration artifacts in Figures 12 and 13 are very similar to those of Claerbout's simple convolutional image condition (8) in Figure 1.

CONCLUSIONS

In this paper, we have compared a number of different imaging conditions for common-shot wave equation migration on a test data set from a vertical-gradient model with four horizontal interfaces. We have seen that different imaging conditions have a different effect on migration artifacts, and may even alter the amplitudes. The most stable of the tested imaging condition divides the up- and downgoing wavefields after inverse Fourier transform. In this way, not only the migration artifacts are strongly reduced, but the amplitudes become more stable and reliable.

Of course, further tests combining some properties of the tested imaging conditions can be conceived of, like the muting of images where the downgoing field is close to zero, which was successful for the cited imaging condition. However, while this would certainly reduce the boundary effects outside the central part of the migrated image, it cannot be expected to improve the behaviour of the amplitudes along the reflector images.

If the amplitudes of wave-equation migration are to be corrected for geometrical-spreading effects in heterogeneous media as suggested by Zhang et al. (2003, 2005), it is important to take the effect of the imaging condition into account.

ACKNOWLEDGMENTS

This research has been supported by FAPESP and CNPq (Brazil), and the sponsors of the Wave Inversion Technology (WIT) consortium.

REFERENCES

Claerbout, J. F. (1971). Toward a unified theory of reflector mapping. *Geophysics*, 36(3):467–481.

Gazdag, J. (1978). Wave equation migration with the phase-shift method. *Geophysics*, 43(07):1342–1351.

Gazdag, J. (1980). Wave equation migration with the accurate space derivative method. *Geophys. Prosp.*, 28(01):60–70.

Guitton, A., Valenciano, A., and Bevc, D. (2006). Robust imaging condition for shot profile migration. In *Expanded Abstracts, 76rd Annual International Meeting*, pages 1059–1062. Soc. of Expl. Geophys.

Sava, P. and Fomel, S. (2006). Time-shift imaging condition on seismic migration. *Geophysics*, 71(6):S209–S217.

Valenciano, A. and Biondi, B. (2003). 2D deconvolution imaging condition for shot profile migration. In *Expanded Abstracts, 73rd Annual International Meeting*, pages 1059–1062. Soc. of Expl. Geophys.

Zhang, Y., Zhang, G., and Bleistein, N. (2003). True amplitude wave equation migration arising from true amplitude one-way wave equations. *Inverse Problems*, 19:1113–1138.

Zhang, Y., Zhang, G., and Bleistein, N. (2005). Theory of true-amplitude one-way wave equations and true-amplitude common-shot migration. *Geophysics*, 70(4):E1–E10.